Construction of synergistic binding sites in a robust MOF for excellent C_2H_4 purification and C_3H_6 recovery performance

Miao Chang[a], Zihan Zhang[a], Changsong Zhuo[b], Ruihan Wang[b,*], Jing Yang[a], Tianlin Ma[a,*], Yuan Fu[a], Yujie Wang[a,*]

[a]School of Materials and Chemical Engineering, Chuzhou University, Chuzhou, 239000, China

[b]Chemical Engineering College, Hebei Normal University of Science and Technology, Qinhuangdao, 066600, China

Corresponding authors.

E-mail addresses: ruihwang@163.com, matianlin951@163.com, wangyj120@chzu.edu.cn.

1. Experimental and theoretical methods

2.1 Reagents and materials

All chemicals are commercially reachable and directly utilized without additional purification handling. Nickel(II) chloride hexahydrate ($NiCl_2 \cdot 6H_2O$), Nickel(II) nitrate hexahydrate ($Ni(NO_3)_2 \cdot 6H_2O$), 1,4-benzenedicarboxylic acid (H_2bdc), 1,4-diazabicyclo [2.2.2] octane (dabco), glycidyl methacrylate (GMA, ≥ 99.0 %), tertbutyl methacrylate (TBMA, ≥ 99.0 %), trimethylolpropane triacrylate (TMPTA, ≥ 99.0 %), poly(ethylene glycol)-block-poly(propylene glycol)-block-poly(ethylene glycol) (P123, Mn = 5800, ≥ 99 %), benzoyl peroxide (BPO, ≥ 99.0 %), ammonium persulfate (APS, 98.5 %), tetraethylenepentamine (TEPA, ≥ 99.0 %), N,N-dimethylaniline (DMA, ≥ 99 %), N, N, N', N'-tetramethylethylenediamine (TMEDA, ≥ 99.0 %), polyvinyl alcohol 1788 (PVA, 80 % hydrolyzed, average Mn, 9000-10000), methanol (MeOH), N, N'-dimethylformamide (DMF) were individually obtained from the Shanghai Tensus Bio-tech Co., Ltd and J&K Scientific Ltd.

2.2 Material synthesis and shaping

Conventional synthesis: The $Ni(bdc)(dabco)_{0.5}$ was synthesized based on the method described in existing literature with slight modifications[1,2]. $NiCl_2 \cdot 6H_2O$ (0.428 g), H_2bdc (0.24 g), and dabco (0.132 g) were mixed with DMF (30 mL) in a 50 mL Teflon-lined steel autoclave, followed by being transferred into the oven and then heated to 393 K for 2 days. The obtained green crystals were washed with DMF and methanol for three days, respectively, during which the crystals were washed with the fresh solvent three times a day. Finally, the material was dried in the vacuum oven at 423 K for 12 h.

Gram-scale synthesis: The gram-scale synthesis of $Ni(bdc)(dabco)_{0.5}$ was completed under reflux environments. $NiCl_2 \cdot 6H_2O$ (10.7 g), H_2bdc (6.0 g), and dabco (3.3 g) were mixed with DMF (1.5 L). Afterward, the mixture was refluxed at 393 K for 2 h. The green powder was collected by filtration. The washing process is the same as conventional synthesis (Yield: 7.96 g, 74.4 % based upon metal salt).

Amino functionalization poly(acrylate) (AFP) synthesis: The AFP was synthesized by the method described in existing literature[3]. First, GMA (2.0 g), TBMA (0.5 g), TMPTA (2.5 g), BPO (0.4 g), and P123 (0.6 g) were dissolved in toluene (8.0 g), and a homogeneous oil

phase was formed by stirring at rotation speed of 400 r min^{-1}. Next, deionized water (20 mL) was slowly dropped into the oil phase, and stirring was continued for 5 minutes. Then, the obtained emulsion was poured into a third phase containing deionized water (150 mL), PVA (1.2 g) and APS (0.8 g), and polymerization was carried out by stirring continuously at 353K for 30 minutes at a rotation speed of 240 r min^{-1}. After the polymerization was completed, poly(acrylate) was collected and dried at 333K for 12 h. After that, the poly(acrylate) was placed in ethanol, soaked at 353 K for 60 minutes to remove P123 from the pores, and dried at 333 K for 12 h. Finally, poly (acrylate) (2.0 g) was placed in TEPA (20.0 g), and grafted at 403 K for 12 h to obtain AFP.

Material shaping: The shaped material was prepared by sequentially impregnating AFP with $Ni(NO_3)_2 \cdot 6H_2O$, dabco and H_2bdc, and growing in situ at 403 K. First, AFP (0.2 g) was put into a solution containing $Ni(NO_3)_2 \cdot 6H_2O$ (2.9 g) and methanol (5 mL), and soaked at 333 K for 2 h. The solution was removed and evaporated in vacuum oven at 403 K for 2 h. Next, the sample was put into a solution containing dabco (0.61 g) and methanol, soaked for 0.5 h at room temperature, and evaporated in a vacuum oven at 403 K for 2 h after the solution was removed again. Then, the sample was put into a solution containing H_2bdc (0.664 g) and DMF (60 mL) and transferred to a Teflon-lined autoclave (100 mL) for reaction at 393 K for 48 h. After the reaction, the sample was washed with DMF and methanol, filtered and dried at 353 K for 12 h, and finally the molded material was obtained.

2.3. Material characterization

Powder X-ray diffraction (PXRD) data were determined based on a D8 Advance X diffractometer equipped with Cu sealed tube. The N_2 adsorption-desorption isotherms at 77 K were estimated through the automatic surface and aperture analyzer (3H-2000PS1 series, Beishide Instrument Technology (Beijing) Co., Ltd). The particle sizes and morphologies were collected by a field-emission scanning electron microscope (FESEM, Hitachi S4700). The thermogravimetric analysis (TGA) was performed using GA Q50-type equipment with an N_2 environment. The Fourier transform infrared (FT-IR) data was measured through a Bruker Vertex 70-type spectrometer.

2.4. Adsorption measurement

The C_3H_6 and C_2H_4 adsorption-desorption isotherms were individually tested using the

BSD-660 M adsorption analyzer (Beishide Instrument Technology Co., Ltd.) at 273 and 298 K. Previous to the test, approximately 1.0 g sample was filled into the sample tube and activated at 423 K with a vacuum degree of 1×10^{-6} bar for 10 h to eliminate the impurities in material pores. During the adsorption test, the corresponding pressure was altered from 0.0 to 1.0 bar and an ice and water bath were used to keep the system temperature constant, respectively. For the new C_3H_6 adsorption-desorption cycle, the activation of the material was achieved by vacuum degassing to 1×10^{-6} bar at room temperature.

2.5. Isosteric heat of adsorption

The isosteric heat of adsorption (Q_{st}) was calculated via the following Clausius-Claperyron equation[4,5]:

$$Q_{st} = \frac{RT_1T_2}{T_1 - T_2} ln \frac{p_2}{p_1} \tag{3}$$

where R, P and T are respectively the gas constant (8.314 J mol^{-1} K^{-1}), test pressure and operation temperature.

2.6. Ideal adsorbed solution theory

The separation selectivity was calculated based upon the ideal adsorbed solution theory (IAST) model after fitting of adsorption isotherms by the following dual-site Langmuir (DSL) expression[6,7]:

$$N_i = N_A^{max} \times \frac{b_A p}{1 + b_A p} + N_B^{max} \times \frac{b_B p}{1 + b_B p} \tag{4}$$

where N_i (unit: cm^3(STP) g^{-1}) signifies the equilibrium uptake of adsorbate i; p (unit: bar) signifies the test pressure on bulk phase; N_A^{max} and N_B^{max} (unit: cm^3(STP) g^{-1}) signify the equilibrium saturated uptake at A and B sites individually; b_A and b_B (unit: bar^{-1} and bar^{-1}) signify the adsorption affinity coefficients at sites A and B individually.

The C_3H_6/C_2H_4 IAST selectivity ($S_{C_3H_6/C_2H_4}$) is as follows:

$$S_{C_3H_6/C_2H_4} = \frac{N_{C_3H_6} / N_{C_2H_4}}{y_{C_3H_6} / y_{C_2H_4}} \tag{5}$$

where $N_{C_3H_6}$ and $N_{C_2H_4}$ are respectively the prediction uptake of the C_3H_8 and C_2H_4 from the

IAST calculation; $y_{C_3H_6}$ and $y_{C_2H_4}$ are respectively the gas molar fraction in the bulk phase.

2.7. Breakthrough test

To evaluate the adsorption and separation performance of this MOF in actual industrial situations, breakthrough tests were executed and the setup diagram is presented in Figure S18. Dried samples (~ 0.4 g) were filled into the stainless-steel adsorption column (Φ 90 × 4.2 mm) with a packed density of 0.62. Before conducting the breakthrough experiment, the sample had been vacuumed and degassed at 423 K for 12 h to remove solvent molecules from the material pores. Then, samples filled within the adsorption column were constantly purged by high-purity helium (He) with a flow rate of 10 mL min^{-1} at 423 K for 2 h to remove the contaminations from the framework pores and the total device. The C_3H_6/C_2H_4 (50/50 and 10/90) mixture was introduced into the adsorption column with a flow rate of 2.0 and 10 mL min^{-1}. The concentration of each gas at the adsorption column outlet was monitored via a mass spectrometer (MS, Hidden, HPR-20). The recyclability of this MOF was finished via durative purging of He flow (10 mL min^{-1} for 2 h) at ambient temperature conditions.

The breakthrough uptake of C_3H_6 was also described based on the following equation.

$$Q_{C_3H_6} = \frac{\int_0^{t_s} (q - q_i)\, dt}{m} \tag{6}$$

$$Q_{C_2H_4} = Q_1 - Q_2 = \frac{q \times t_1 - \left(\int_0^{t_1} q_i\, dt\right) + \left(\int_{t_1}^{t_2} q_i\, dt - q \times (t_2 - t_1)\right)}{m} \tag{7}$$

where $Q_{C_3H_6}$ and $Q_{C_2H_4}$ are the C_3H_6 and C_2H_4 breakthrough uptake (cm^3(STP) g^{-1}), respectively; q and q_i are feed flow rate and the flow rate (mL min^{-1}) at time t (min), respectively; t_s, t_1, and t_2 (min) are the time of C_3H_6 adsorption saturation, the time when the C_2H_4 outlet concentration is equal to the feed concentration, and the time of C_2H_4 adsorption saturation during thebreakthrough experiment; m represents the quality of adsorbent (g).

The C_2H_4 productivity ($q_{C_2H_4}$) is defined by the breakthrough uptake of C_2H_4, which is calculated by integration of the breakthrough curves *f(t)* during a period from t_3 to t_4 when the C_2H_4 purity is higher than or equal to a threshold value (99.95 %)[8,9] (Figures S21 and S26).

The productivity of C_2H_4 is calculated by the following equation.

$$q_{C_2H_4} = \frac{c_i(C_2H_4)}{c_i(C_2H_4)+c_i(C_3H_6)} \times \left(\int_{t_3}^{t_4} f(t)dt\right) \quad (8)$$

where c_i represents the concentration (mol L^{-1}) of the *i* guest molecules at the outlet of the adsorption

2.8. Computational methodology

Grand Canonical Monte Carlo (GCMC) simulations were conducted using the RASPA-2.0 software package[10]. The simulation protocol consisted of an initial equilibration phase of 10^5 steps, followed by 10^5 production steps. The gas molecules were represented as single-site beads, and the coordinates of the Ni(bdc)(dabco)$_{0.5}$ structure were kept fixed throughout the GCMC simulation. A spherical cutoff of 14 Å with a long-range correction was used to calculate the Lennard–Jones interactions. The atoms in the Ni(bdc)(dabco)$_{0.5}$ framework were assigned using the Universal Force Field[11] and the Transferable Potentials for Phase Equilibria (TraPPE) force field[12] for the C_3H_6 and C_2H_4 molecules. The supercell was constructed by replicating the unit cell in all three dimensions, with a 2 × 2 × 4 expansion.

The primitive Ni(bdc)(dabco)$_{0.5}$ structure was optimized in the periodic density functional theory (DFT) calculations. All DFT calculations were performed using the CP2K package (version 2021.3)[13], employing the Perdew-Burke-Ernzerhof functional and a hybrid plane-wave/Gaussian basis set. The valence electron wavefunction was expanded using a double-ζplus polarization basis set (DZVP-MOLOPT-SR-GTH), while Goedecker–Teter–Hutter (GTH) pseudopotentials were applied for the core electrons[14,15]. Dispersion corrections were incorporated in all DFT calculations using the Grimme-D3 method[16]. The binding energy E_b of each adsorption site was calculated via the subsequent equation:

$$E_b = E_{gas+MOF} - E_{MOF} - E_{gas} \quad (9)$$

where $E_{gas+MOF}$ represents the energy of optimized gas+MOF species, E_{MOF} and E_{gas} are individually the energies of optimized empty framework and the solitary adsorbate molecule. Independent Gradient Model (IGM) was analyzed using Multiwfn[17,18], and the visualization was carried out with VMD[19].

2. Material characterization

Table S1. Summary of physical parameters of C_3H_6 and C_2H_4.

Gases	Kinetic diameter (Å)	Critical temperature (K)	Dipole moment ($\times 10^{-30}$ C m)	Quadrupole moment ($\times 10^{-40}$ C m^2)	Polarizability ($\times 10^{-25}$ cm^3)
C_3H_6	4.163	364.9	1.22	—	62.6
C_2H_4	4.678	282.3	0	5.0	42.5

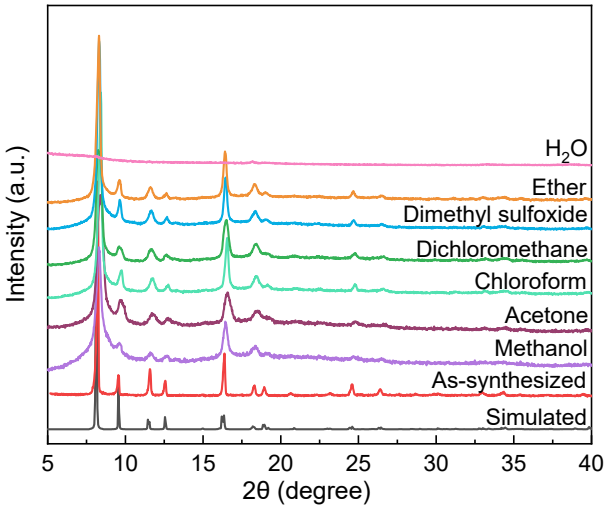

Figure S1. PXRD of materials treated with different solvents.

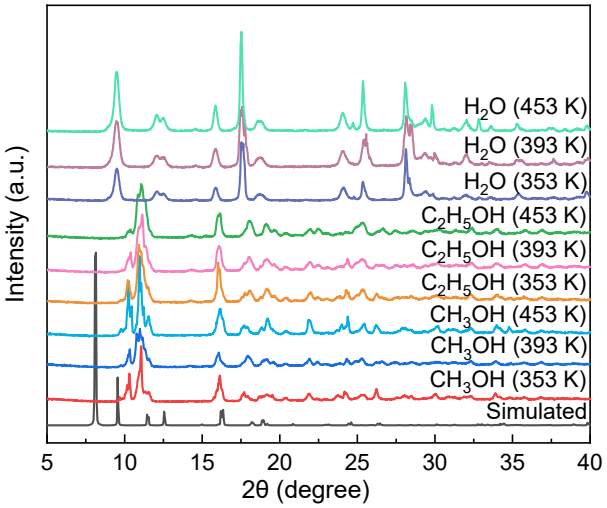

Figure S2. Comparison of PXRD between materials synthesized using different solvents and simulated $Ni(bdc)(dabco)_{0.5}$.

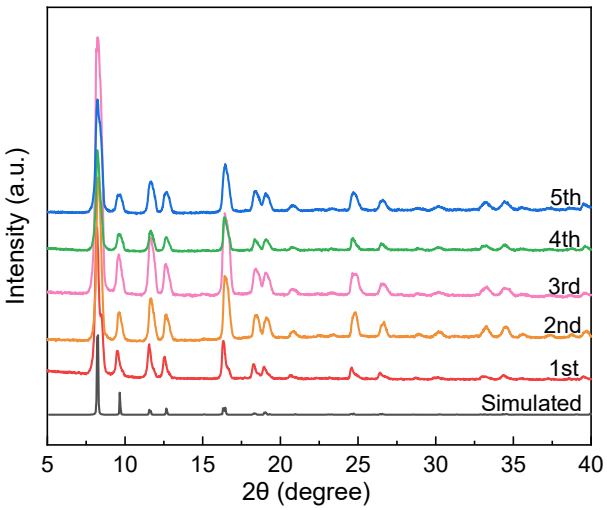

Figure S3. PXRD of synthesis of Ni(bdc)(dabco)$_{0.5}$ using recycled DMF solvents.

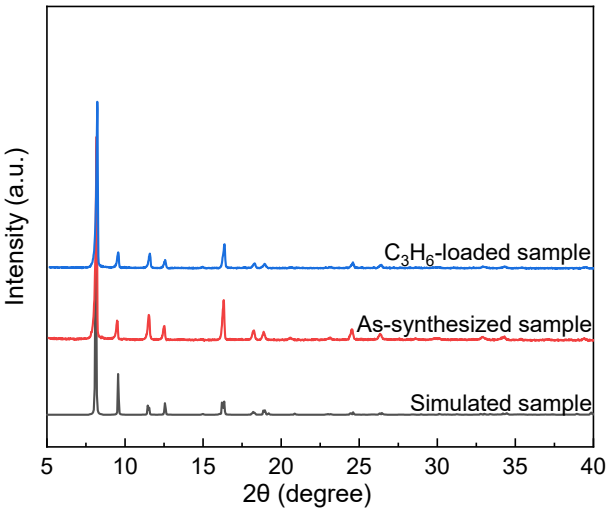

Figure S4. PXRD of as-synthesized and C_3H_6-loaded Ni(bdc)(dabco)$_{0.5}$.

Table S2. Slope, intercept, BET constant, and R^2 of Ni(bdc)(dabco)$_{0.5}$.

MOF	Slope	Intercept	BET constant	R^2
Ni(bdc)(dabco)$_{0.5}$	0.00229	3.9373×10^{-7}	2269.0	0.9995

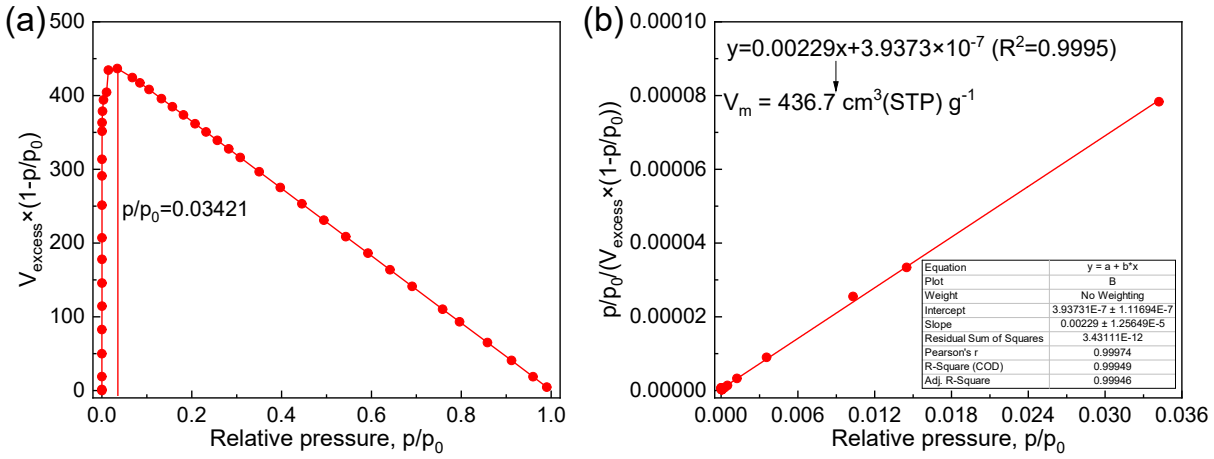

Figure S5. BET surface area calculation for the Ni(bdc)(dabco)$_{0.5}$ using the simulated isotherm of N_2 at 77 K. (a) plot of V_{excess}×(1-p/p_0) vs P/P_0 for the determination using the first consistency criterion, (b) the selected linear plot that satisfies the second consistency criterion and the corresponding BET surface area from the linear fit.

Table S3. Pore size, BET surface area, and pore volume of Ni(bdc)(dabco)$_{0.5}$.

MOF	Pore size (Å)	BET surface area (m^2 g^{-1})	Pore volume (cm^3 g^{-1})
Ni(bdc)(dabco)$_{0.5}$	7.8[a]	1899.6[b]	0.71[c]

[a] Calculated by HK model.

[b] Calculated from N_2 adsorption isotherms at 77 K in the range of P/P_0 = 2×10^{-9}-0.03421.

[c] Calculated by NLDFT model.

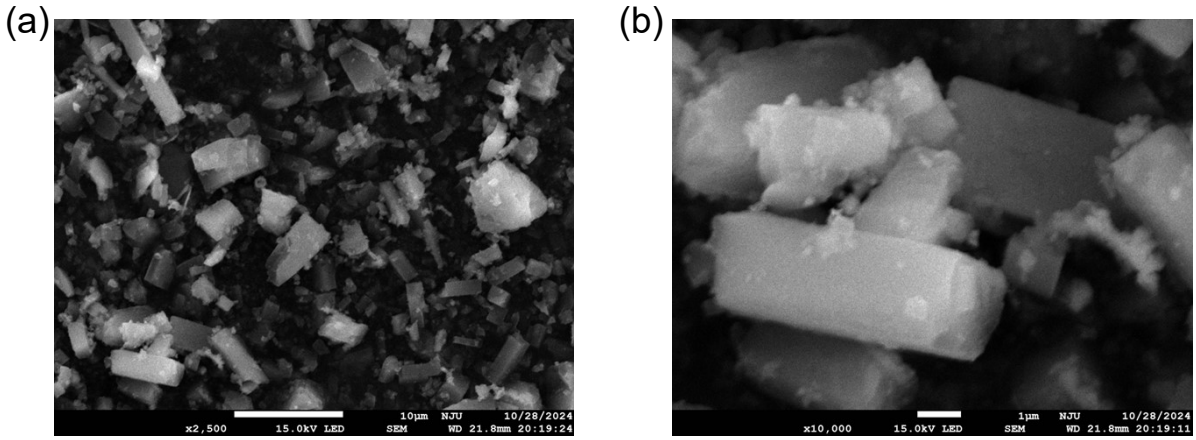

Figure S6. FESEM image of Ni(bdc)(dabco)$_{0.5}$.

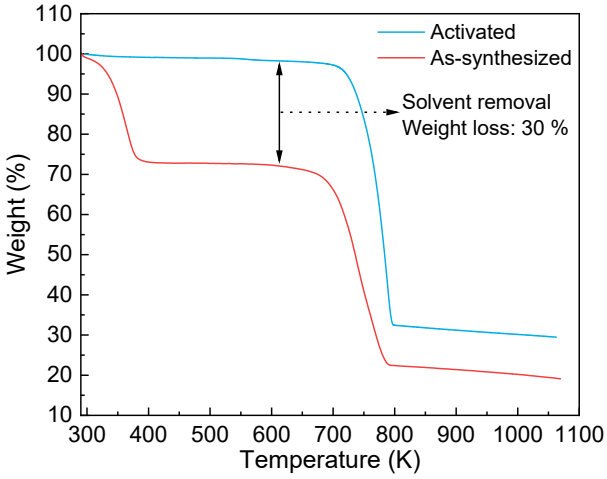

Figure S7. The TGA curve of Ni(bdc)(dabco)$_{0.5}$.

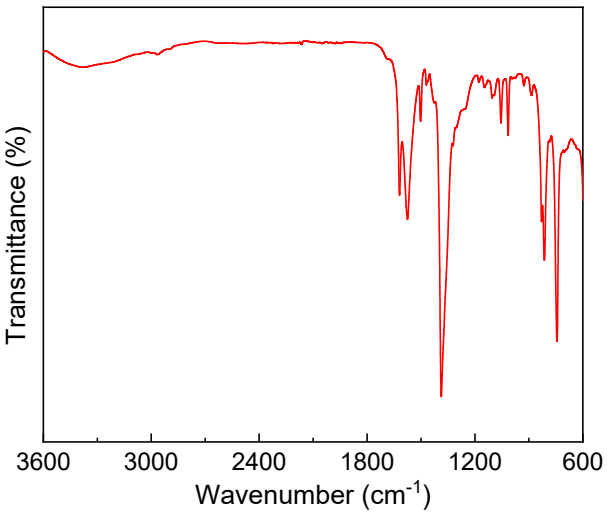

Figure S8. The FT-IR of Ni(bdc)(dabco)$_{0.5}$.

3. Experimental data for gas adsorption

3.1. Adsorption isotherms fitting and selectivity calculation

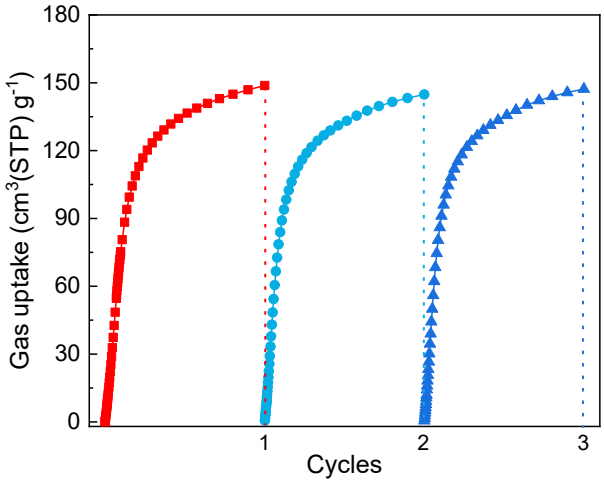

Figure S9. Cyclic experiments for C_3H_6 adsorption in Ni(bdc)(dabco)$_{0.5}$.

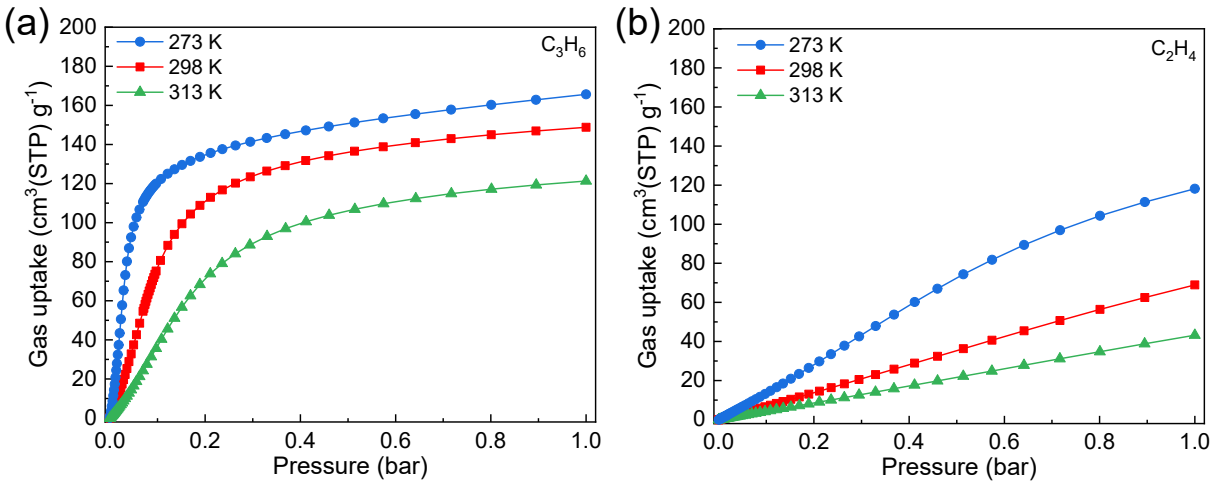

Figure S10. The single-component adsorption isothermals of C_3H_6 and C_2H_4 in Ni(bdc)(dabco)$_{0.5}$ at 273, 298, and 313 K.

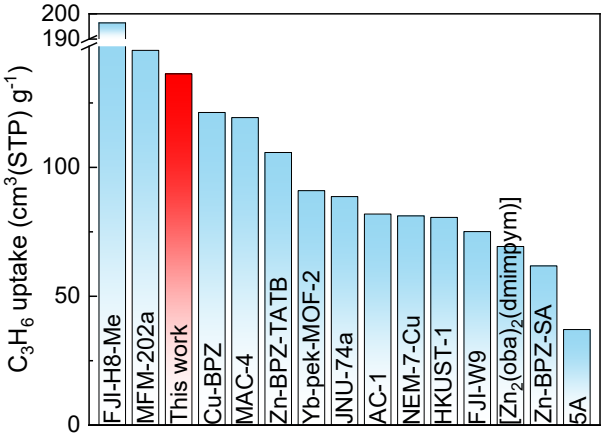

Figure S11. Comparison of the C_3H_6 uptake of Ni(bdc)(dabco)$_{0.5}$ with so far reported high-performance materials at 0.5 bar.

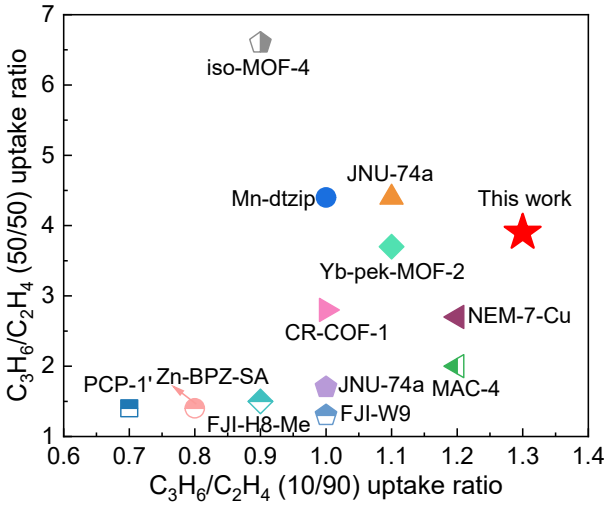

Figure S12. Comparison of the C_3H_6/C_2H_4 (10/90 and 50/50) uptake ratio of Ni(bdc)(dabco)$_{0.5}$ with so far reported high-performance materials.

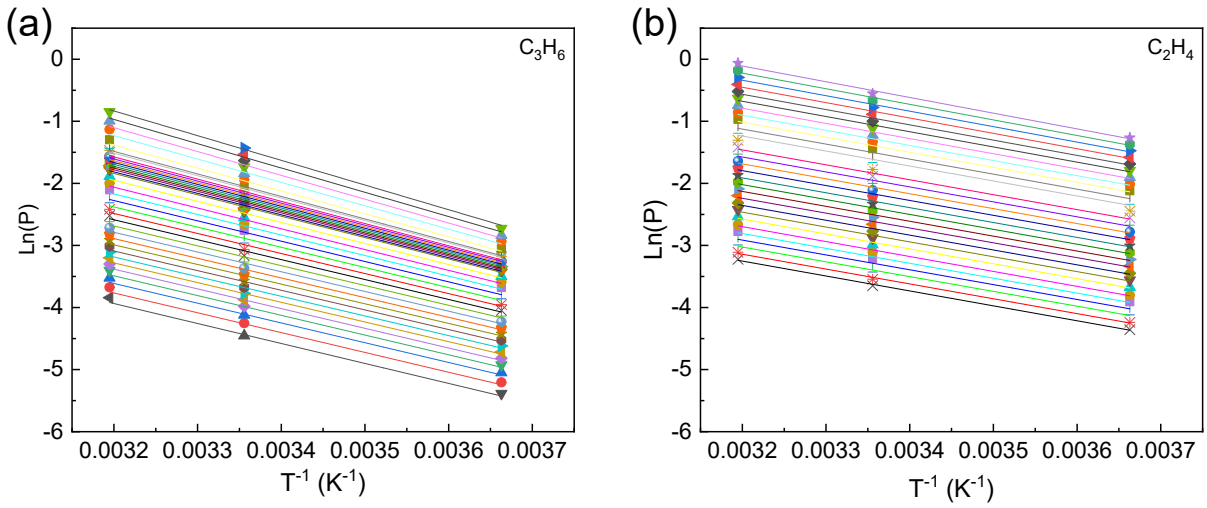

Figure S13. The isostere plots of C_3H_6 (a) and C_2H_4 (b) of Ni(bdc)(dabco)$_{0.5}$.

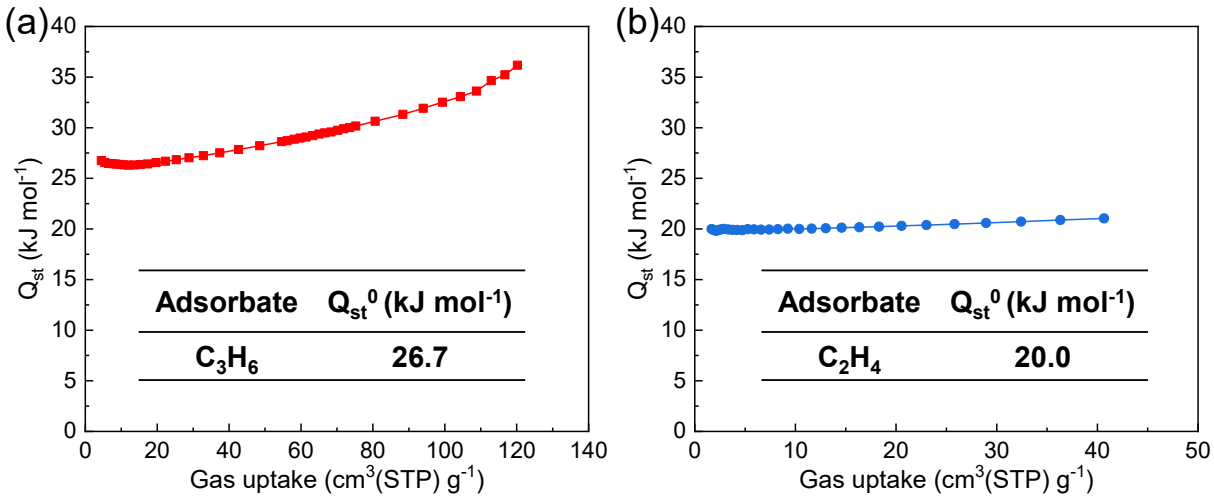

Figure S14. Isosteric heat of adsorptions of C_3H_6 (a) and C_2H_4 (b) in Ni(bdc)(dabco)$_{0.5}$ derived from Clausius-Clapeyron equation, as a function of adsorption loading.

Table S4. The fitting parameters by the DSL model based on the pure component isotherms data of C_3H_6 and C_2H_4 in Ni(bdc)(dabco)$_{0.5}$ at 298 K.

Gases	*Nmax A* (cm^3(STP) g^{-1})	b_A $_{bar^{-1}}$	*Nmax B* (cm^3(STP) g^{-1})	b_B $_{bar^{-1}}$
C_3H_6	0.3707	8.1328	170.0822	8.1328
C_2H_4	183.8290	0.2787	121.1110	0.2787

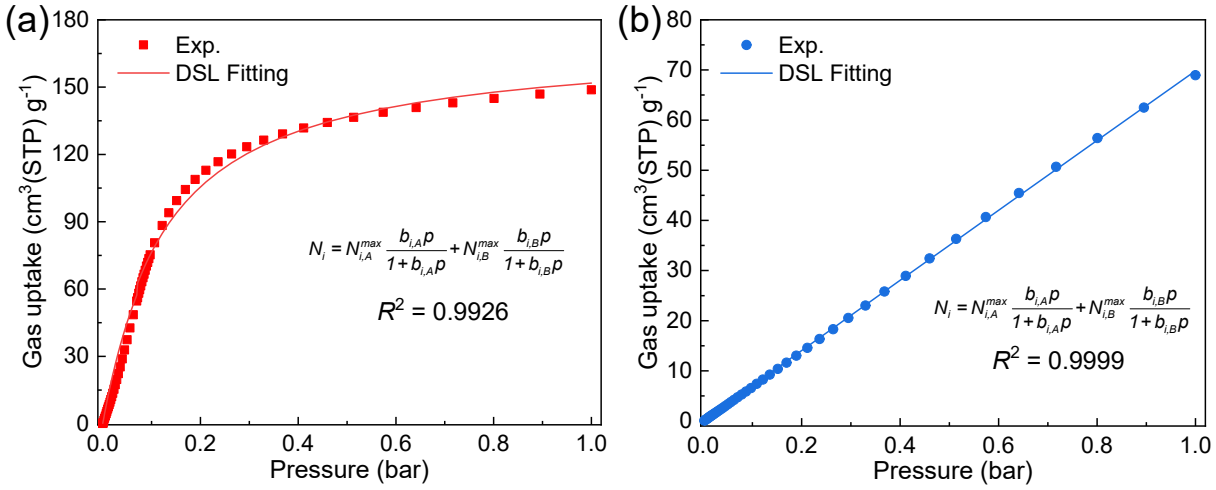

Figure S15. The DSL model for fitting C_3H_6 (a) and C_2H_4 (b) isotherm of Ni(bdc)(dabco)$_{0.5}$ at 298 K.

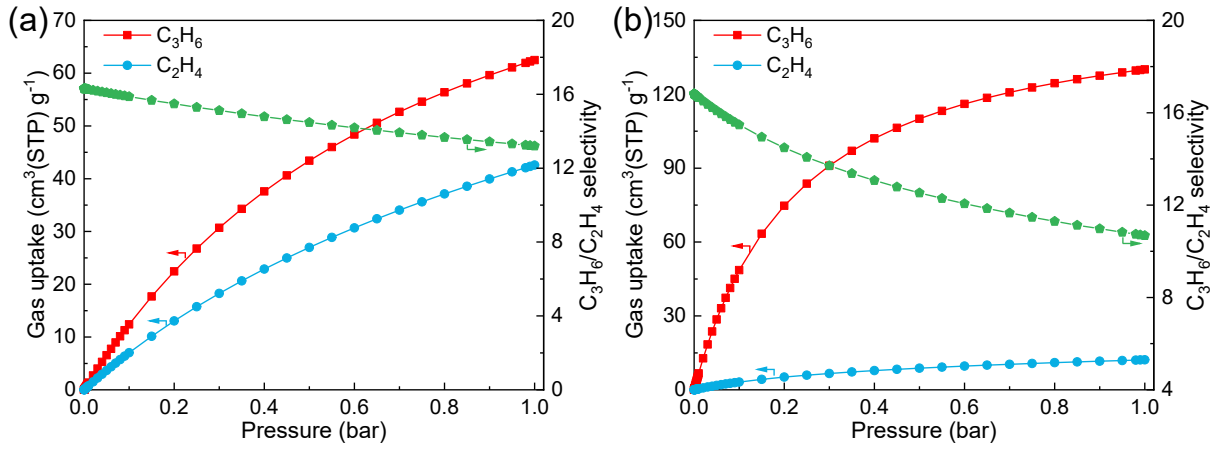

Figure S16. The adsorption isotherm of C_3H_6 (C_2H_4) and the C_3H_6/C_2H_4 selectivity predicted from IAST in Ni(bdc)(dabco)$_{0.5}$ at 298 K, as function of the pressure. (a) C_3H_6/C_2H_4 = 10/90; (b) C_3H_6/C_2H_4 = 50/50.

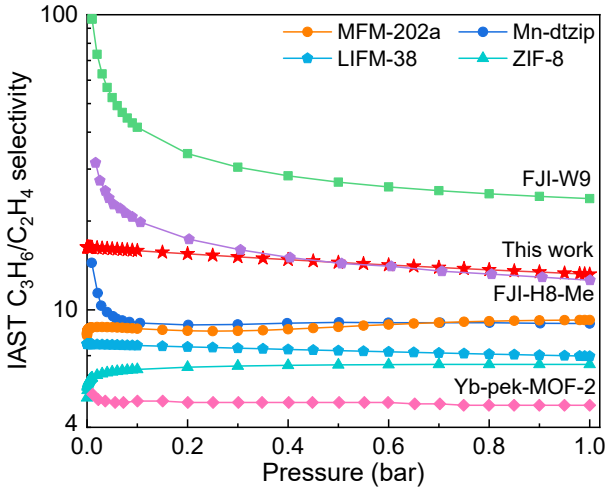

Figure S17. Comparison of the C_3H_6/C_2H_4 (10/90) selectivity of Ni(bdc)(dabco)$_{0.5}$ with thus far reported advanced adsorbents at 298 K and 0.0-1.0 bar.

4. Results of breakthrough experiment of C_3H_6/C_2H_4 mixture

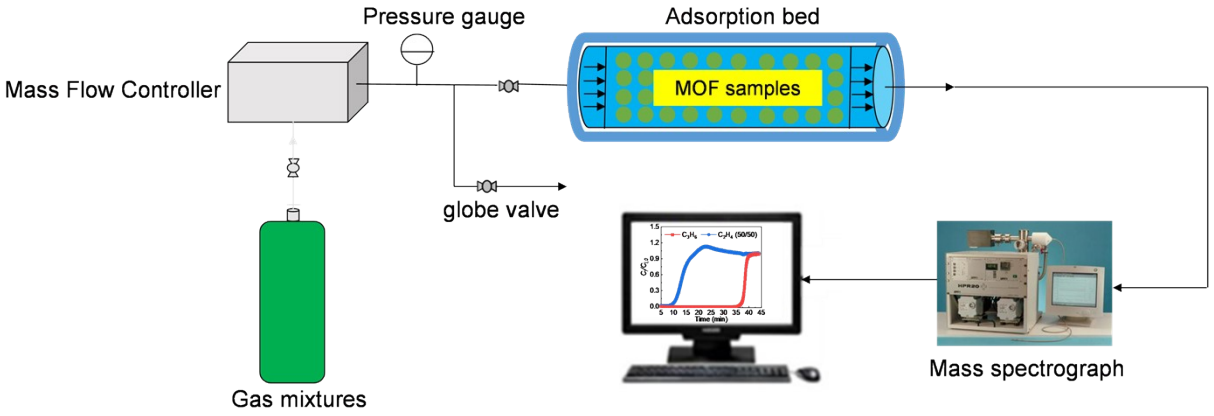

Figure S18. The experimental setup of mixed gases breakthrough test.

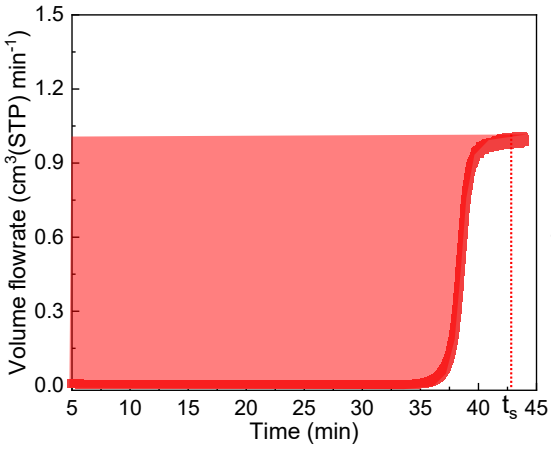

Flow rate of C_3H_6 (50 %):

q = 1.0 cm^3(STP) min^{-1}.

The maximum uptake of C_3H_6 during the time interval 0-t_s:

$$Q_{C_3H_6} = \frac{\int_0^{t_s} (q - q_i)\, dt}{m} = 101.2 \text{ cm}^3\text{(STP) g}^{-1}.$$

Figure S19. Calculation of the C_3H_6 uptake in Ni(bdc)(dabco)$_{0.5}$ from a breakthrough experiment performed on an equimolar C_3H_6/C_2H_4 (50/50) mixture.

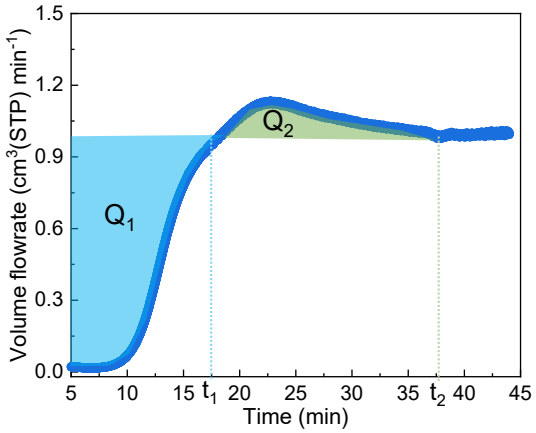

Flow rate of C_2H_4 (50 %):

q = 1.0 cm^3(STP) min^{-1}.

The maximum uptake of C_2H_4 during the time interval 0-t_2:

$$Q_{C_2H_4} = Q_1 - Q_2 = \frac{q \times t_1 - \left(\int_0^{t_1} q_i\, dt\right)\left(\int_{t_1}^{t_2} q_i\, dt - q \times (t_2 - t_1)\right)}{m} = 30.3 \text{ cm}^3\text{(STP) g}^{-1}.$$

Figure S20. Calculation of the C_2H_4 uptake in Ni(bdc)(dabco)$_{0.5}$ from a breakthrough experiment performed on an equimolar C_3H_6/C_2H_4 (50/50) mixture.

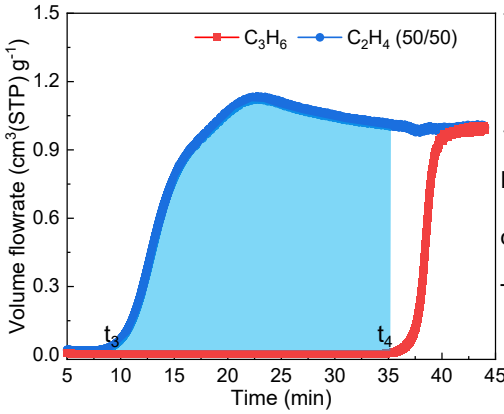

The C_2H_4 productivity was calculated by integration of the C_2H_4 breakthrough curves q(t). The C_2H_4 purity is higher or equal to a threshold value (≥ 99.95) during the integration interval from t_3 to t_4

Flow rate of C_2H_4 (50 %):

q = 1.0 cm^3(STP) min^{-1}.

The maximum C_2H_4 productivity during the time interval t_3-t_4:

$$q_{C_2H_4} = \frac{c_i(C_2H_4)}{c_i(C_2H_4)+c_i(C_3H_6)} \times \left(\int_{t_3}^{t_4} f(t)dt\right)$$ = 57.3 cm^3(STP) g^{-1}.

Figure S21. Calculation of the C_2H_4 productivity in Ni(bdc)(dabco)$_{0.5}$ from a breakthrough experiment performed on an equimolar C_3H_6/C_2H_4 (50/50) mixture.

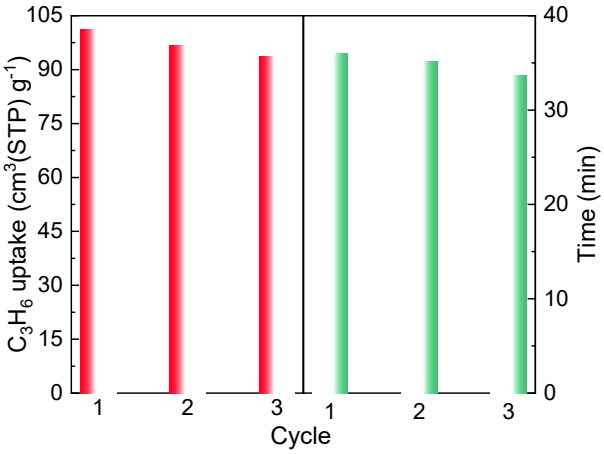

Figure S22. The cycle breakthrough uptake and time of C_3H_6 on Ni(bdc)(dabco)$_{0.5}$.

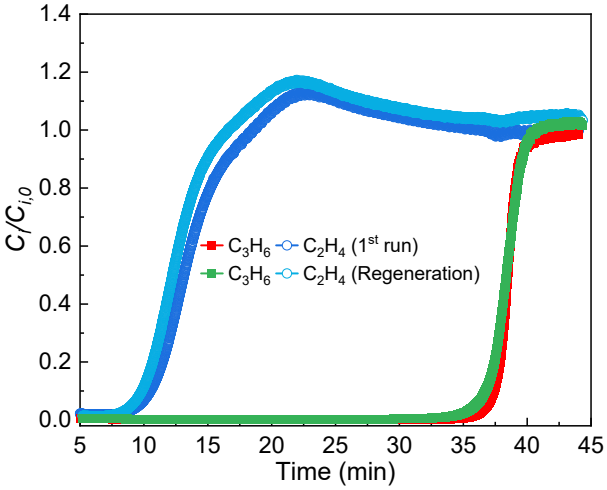

Figure S23. Breakthrough tests of regenerated Ni(bdc)(dabco)$_{0.5}$ toward the equimolar C_3H_6/C_2H_4 (50/50) mixture at 298 K.

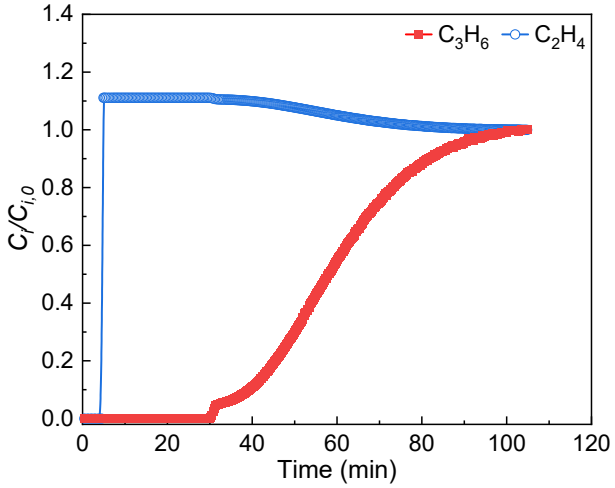

Figure S24. Breakthrough tests of Ni(bdc)(dabco)$_{0.5}$ toward the C_3H_6/C_2H_4 (10/90) mixture at 298 K and 1.0 bar.

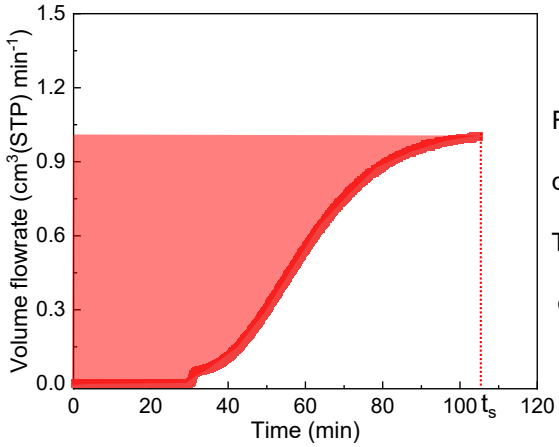

Flow rate of C_3H_6 (50 %):

q = 1.0 cm^3(STP) min^{-1}.

The maximum uptake of C_3H_6 during the time interval 0-t_s:

$$Q_{C_3H_6} = \frac{\int_0^{t_s}(q - q_i)\,dt}{m} = 62.9 \text{ cm}^3\text{(STP) g}^{-1}.$$

Figure S25. Calculation of the C_3H_6 uptake in Ni(bdc)(dabco)$_{0.5}$ from a breakthrough experiment performed on a C_3H_6/C_2H_4 (10/90) mixture.

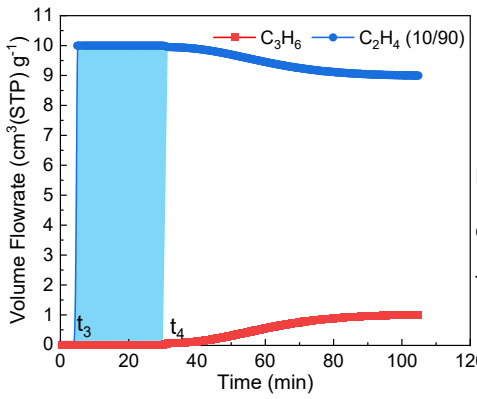

The C_2H_4 productivity was calculated by integration of the C_2H_4 breakthrough curves q(t). The C_2H_4 purity is higher or equal to a threshold value (≥ 99.95) during the integration interval from t_3 to t_4

Flow rate of C_2H_4 (90 %):

q = 9.0 cm^3(STP) min^{-1}.

The maximum C_2H_4 productivity during the time interval t_3-t_4:

$$q_{C_2H_4} = \frac{c_i(C_2H_4)}{c_i(C_2H_4) + c_i(C_3H_6)} \times \left(\int_{t_3}^{t_4} f(t)dt\right) = 265.8 \text{ cm}^3\text{(STP) g}^{-1}.$$

Figure S26. Calculation of the C_2H_4 productivity in Ni(bdc)(dabco)$_{0.5}$ from a breakthrough experiment performed on a C_3H_6/C_2H_4 (10/90) mixture.

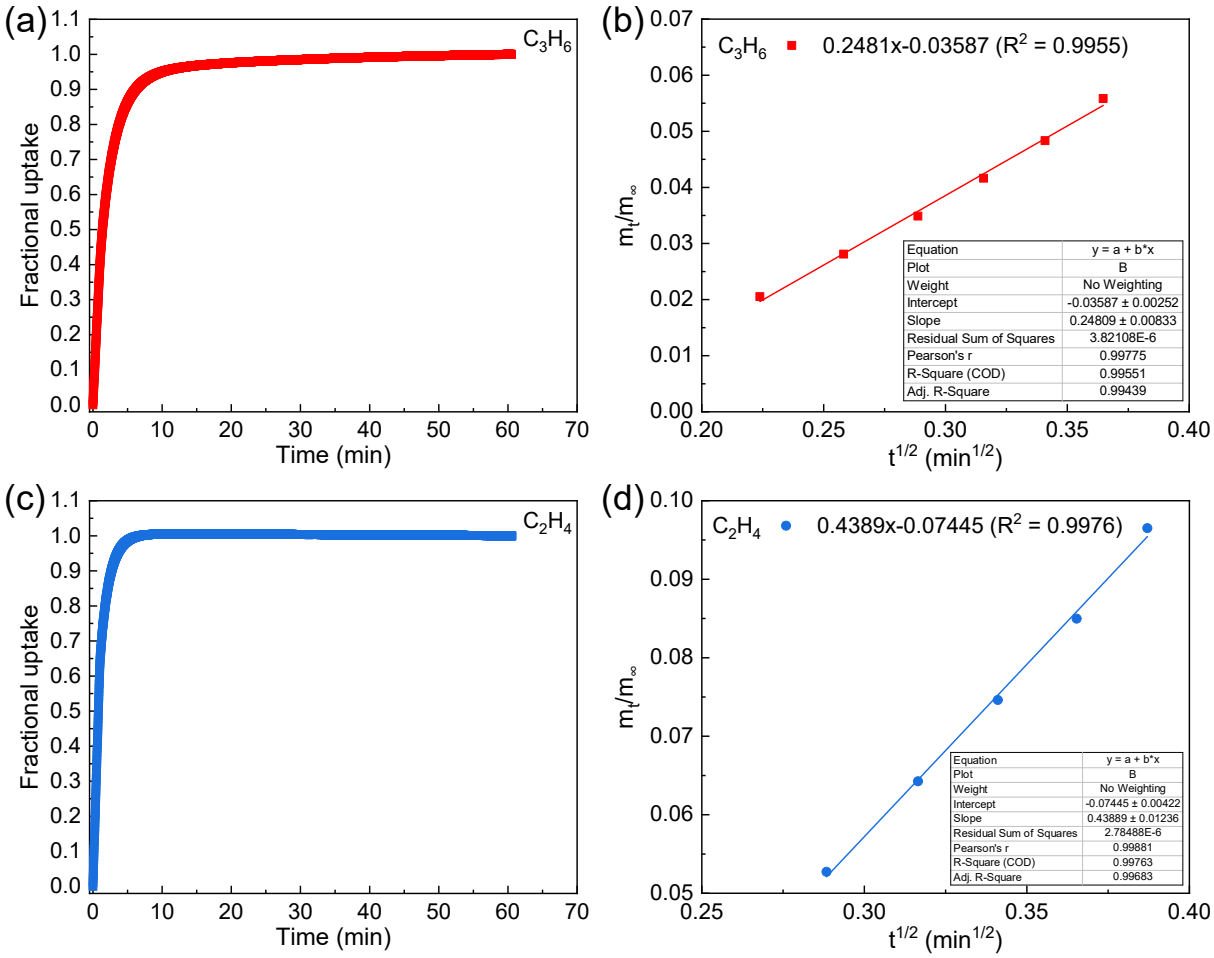

Figure S27. Time-dependent gas uptake profiles of C_3H_6 and C_2H_4 on Ni(bdc)(dabco)$_{0.5}$ at 298 K and 0.5 bar (a, c) and the corresponding fitting of diffusion time constants based on time-dependent gas uptake profiles of C_3H_6 and C_2H_4 (b, d).

5. Theoretical calculations

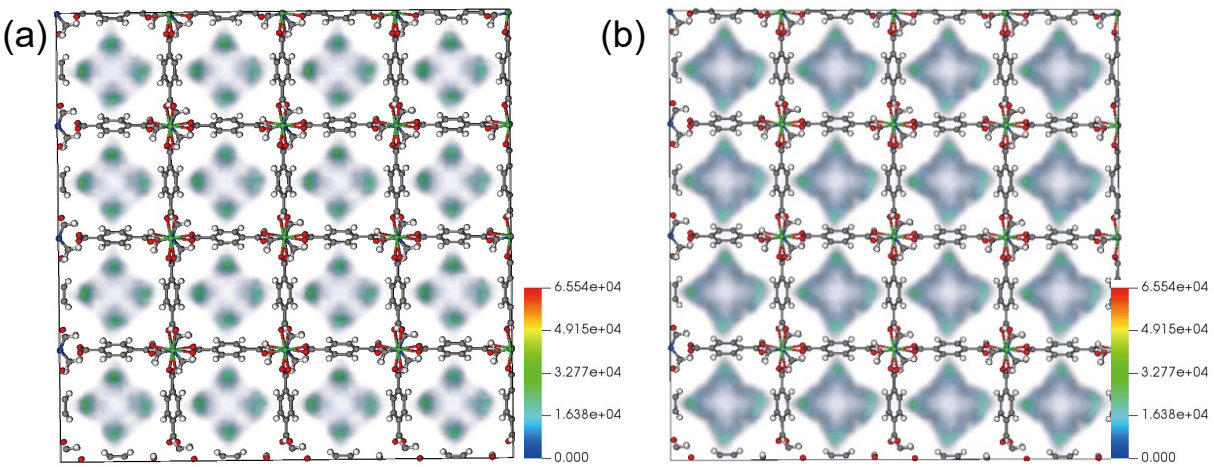

Figure S28. COM probability density distributions of C_3H_6 (a) and C_2H_4 (b) molecules by GCMC simulation in Ni(bdc)(dabco)$_{0.5}$ at 298 K and 1.0 bar.

6. Comparison of separation properties

Table S5. Comparison of adsorptive separation performance of $Ni(bdc)(dabco)_{0.5}$ with the selected various porous adsorbents reported in literature, including C_3H_6 (0.1, 0.5, 1.0 bar and 298 K), C_2H_4 (0.1, 0.5, 0.9, 1.0 bar and 298 K) uptake, and C_3H_6/C_2H_4 (0.1/0.1, 0.1/0.9, and 0.5/0.5) uptake ratio.

Adsorbents	C_3H_6 uptake ($cm^3(STP)\ g^{-1}$)			C_2H_4 uptake ($cm^3(STP)\ g^{-1}$)				C_3H_6/C_2H_4 uptake ratio			Refs
	0.1 bar	0.5 bar	1.0 bar	0.1 bar	0.5 bar	0.9 bar	1.0 bar	0.1 /0.1	0.1 /0.9	0.5 /0.5	
FJI-H8-Me	156.1	196.4	211.0	56.6	133.1	167.3	173.1	2.8	0.9	1.5	[20]
MAC-4	93.5	119.3	127.0	24.0	58.2	78.5	83	3.8	1.2	2.0	[21]
$Ni(bdc)(dabco)_{0.5}$	**80.6**	**136.3**	**148.8**	**7.4**	**35.1**	**62.5**	**68.9**	**10.9**	**1.3**	**3.9**	**This work**
Zn-BPZ-TATB	80.0	105.8	114.0	16.8	64.4	87.3	17.3	4.8	0.9	1.6	[22]
Mn-dtzip	68.9	181.1	216.4	10.6	40.7	69.8	76.7	6.5	1.0	4.4	[23]
JNU-74a	68.5	88.7	94.6	19.5	51.6	68.3	71.5	3.5	1.0	1.7	[24]
FJI-W9	63.0	75.1	83.0	29.9	56.3	65.2	66.0	2.1	1.0	1.3	[25]
MFM-202a	62.5	145.4	160.8	6.9	32.8	58.5	65.0	9.1	1.1	4.4	[26]
$[Zn_2(oba)_2(dmimpym)]$	53.6	69.3	76.0	8.3	33.5	46.1	48.3	6.5	1.2	2.1	[27]
iso-MOF-4	52.4	214.3	254.5	6.7	32.3	59.7	70.0	7.8	0.9	6.6	[28]
Zn-BPZ-SA	46.6	61.8	68.3	11.8	43.4	60.8	63.9	3.9	0.8	1.4	[29]
Cu-BPZ	45.8	121.3	138.0	6.1	28.4	47.4	52.0	7.5	1.0	4.3	[30]
Yb-pek-MOF-2	40.9	91.0	127.3	5.5	24.3	38.5	41.7	7.4	1.1	3.7	[31]
PCP 1'	37.8	60.0	70.7	20.1	42.4	54.5	56.7	1.9	0.7	1.4	[32]
CR-COF-1	35.6	71.2	84.0	7.9	25.2	36.3	38.0	4.5	1.0	2.8	[33]
spe-MOF	35.5	162.9	236.9	6.2	26.6	44.8	48.9	5.7	0.8	6.1	[34]
$[Cd_2(AzDC)_2(TPT)_2]$	35.2	54.5	59.8	10.9	29.7	39.2	45.0	3.2	0.9	1.8	[35]
NEM-7-Cu	55.7	81.2	87.9	8.3	29.9	44.6	47.8	6.7	1.2	2.7	[36]
UPC-33	24.0	74.7	94.3	3.6	15.6	26.5	31.1	6.7	0.9	4.8	[37]
LIFM-38	15.0	42.2	58.0	2.1	10.8	18.5	19.9	7.1	0.8	3.9	[38]
AC-1	15.1	81.9	122.4	3.9	19.0	31.6	34.3	3.9	0.5	4.3	[39]
HKUST-1	14.4	80.6	105.9	7.1	30.4	45.3	48.1	2.0	0.3	2.7	[39]
ZIF-8	13.0	54.1	71.1	1.2	9.3	18.3	20.5	10.8	0.7	5.8	[39]
MIL-101-Cr	12.4	70.6	124.5	3.5	16.4	28.4	31.2	3.5	0.4	4.3	[39]
5A	7.4	37.1	49.5	6.1	23.3	29.9	30.8	1.2	0.2	1.6	[39]
13X	2.0	6.4	9.1	1.3	4.5	6.6	7.1	1.5	0.3	1.4	[39]

Table S6. Comparison of adsorptive separation performance of $Ni(bdc)(dabco)_{0.5}$ with the selected various porous adsorbents reported in literature, including C_3H_6/C_2H_4 (0.1/0.9 and 0.5/0.5) selectivity and Q0 st of C_3H_6 and C_2H_4.

Adsorbents	Selectivity C_3H_6/C_2H_4 (10/90)	Selectivity C_3H_6/C_2H_4 (50/50)	Q0 st (kJ mol^{-1})		Refs
			C_3H_6	C_2H_4	
FJI-H8-Me	12.6	9.9	44.3	34.3	[20]
MAC-4	10.6	9.5	25.3	17.1	[21]
$Ni(bdc)(dabco)_{0.5}$	**13.2**	**10.7**	**26.7**	**20.0**	**This work**
Zn-BPZ-TATB	8.9	7.4	28.1	18.3	[22]
Mn-dtzip	9.0	8.6	35.1	24.6	[23]
JNU-74a	16.9	13.0	36.2	22.5	[24]
FJI-W9	23.8	20.5	38.0	20.9	[25]
MFM-202a	9.2	8.4	33.0	18.0	[26]
$[Zn_2(oba)_2(dmimpym)]$	17.1	15.6	33.3	25.8	[27]
iso-MOF-4	7.2	7.7	30.9	25.4	[28]
Zn-BPZ-SA	6.1	4.8	33.7	23.1	[29]
Cu-BPZ	7.4	7.4	30.3	20.7	[30]
Yb-pek-MOF-2	5.4	4.8	34.0	27.3	[31]
PCP 1'	4.4	3.6	14.8	24.7	[32]
CR-COF-1		11.2	29.8	26.0	[33]
spe-MOF	6.7	7.7	29.4	22.5	[34]
$[Cd_2(AzDC)_2(TPT)_2]$	10.2	1.2	42.1	30.6	[35]
NEM-7-Cu	8.5	8.6	36.9	22.5	[36]
UPC-33	5.8	5.7	48.9	10.31	[37]
LIFM-38	7.0	6.4	27.3	28.1	[38]
AC-1	4.2	5.0			[39]
HKUST-1	2.7	3.1			[39]
ZIF-8	6.5	6.4			[39]
MIL-101-Cr	3.9	4.3			[39]
5A	1.6	1.8			[39]
13X	1.7	1.7			[39]

6. Shaping of MOF

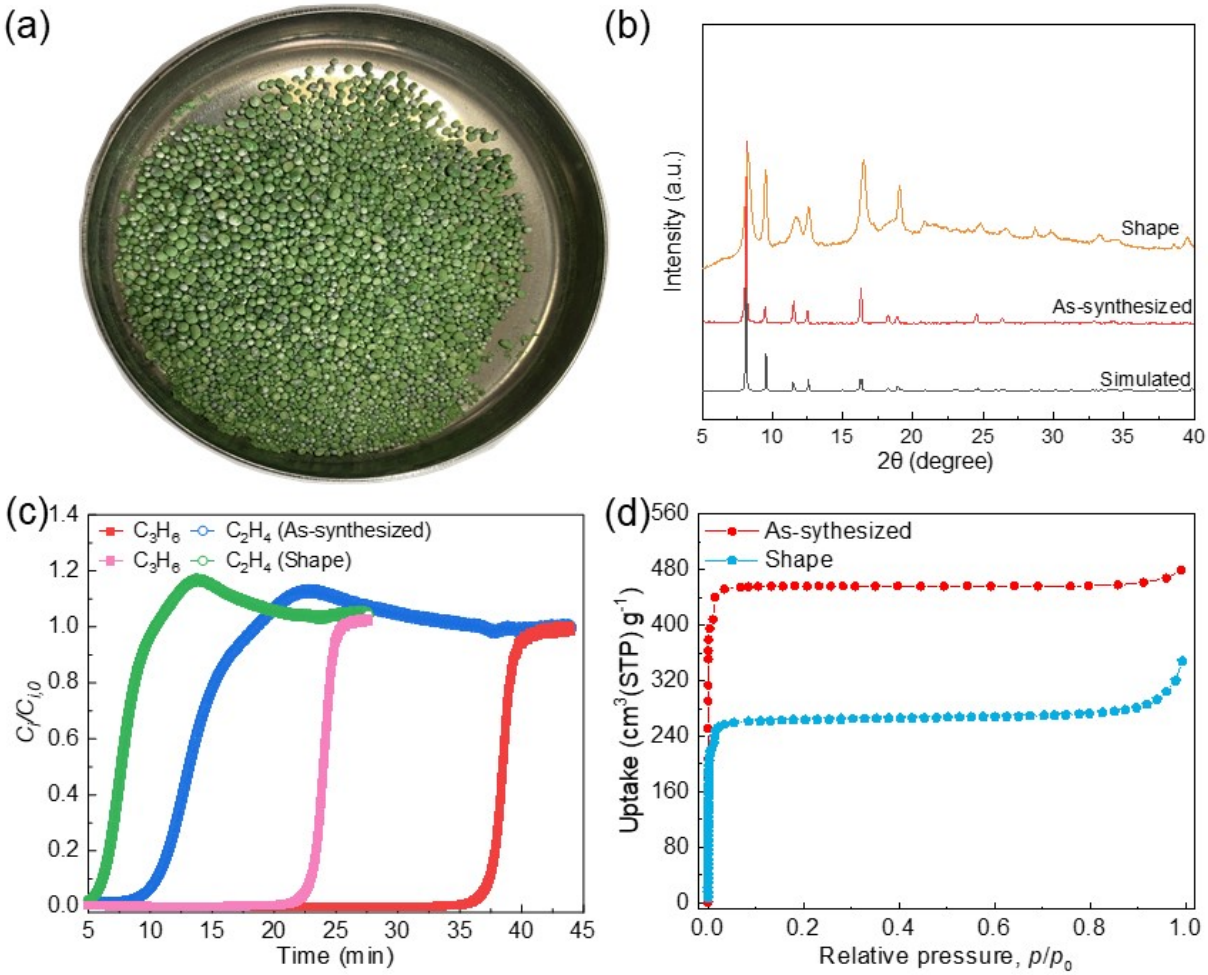

Figure S29. (a) Photographs of shaped Ni(bdc)(dabco)$_{0.5}$. (b) The PXRD pattern and (c) breakthrough tests of equimolar C_3H_6/C_2H_4 (50/50) mixture at 298 K as well as (d) the N_2 adsorption curve at 77 K of shape and as-synthesized Ni(bdc)(dabco)$_{0.5}$.

Table S7. The estimated price of synthesis of $Ni(bdc)(dabco)_{0.5}$ and some benchmark materials.

MOFs	Raw Materials	Price	Source	Total cost of MOFs	Refs
$Ni(bdc)(dabco)_{0.5}$	$NiCl_2·6H_2O$	0.025 \$ g^{-1}	Greagent	3.44 \$ g^{-1}	**This work**
	H_2BDC	0.0066 \$ g^{-1}	Adamas		
	dabco	0.022 \$ g^{-1}	Adamas		
	DMF	0.018 \$ mL^{-1}	Sigma-Aldrich		
ZJU-74-Pd	$K_2[Pd(CN)_4]·3H_2O$	292.5 \$ mL^{-1}	Adamas	675.4 \$ g^{-1}	[40]
	$Co(NO_3)_2·6H_2O$	0.039 \$ g^{-1}	Greagent		
	pyrazine	0.10 \$ g^{-1}	Adamas		
	CH_3OH	0.0031 \$ mL^{-1}	Sigma-Aldrich		
FJI-W9	$YCl_3·6H_2O$	0.026 \$ g^{-1}	Greagent	196.6 \$ g^{-1}	[25]
	H_4L	69.4 \$ g^{-1}	Adamas		
	2-fluorobenzoic acid	0.024 \$ g^{-1}	Adamas		
	DMF	0.018 \$ mL^{-1}	Sigma-Aldrich		
MAC-4	$Zn(OAc)_2·2H_2O$	0.003 \$ g^{-1}	Greagent	1.35 \$ g^{-1}	[21]
	Hdmtrz	2.469 \$ g^{-1}	Adamas		
	H_2IPA	0.007 \$ g^{-1}	Adamas		
	DMF	0.018 \$ mL^{-1}	Sigma-Aldrich		
Zn-BPZ-SA	$Zn(NO_3)_2·6H_2O$	0.055 \$ g^{-1}	Greagent	70.0 \$ g^{-1}	[29]
	H_2BPZ	52.1 \$ g^{-1}	Adamas		
	H_2SA	1.3 \$ g^{-1}	Adamas		
	DMF	0.018 \$ mL^{-1}	Sigma-Aldrich		
Zn-BPZ-TATB	$ZnCl_2$	0.014 \$ g^{-1}	Greagent	257.6 \$ g^{-1}	[22]
	TATB	23.2 \$ g^{-1}	Adamas		
	H_2BPZ	52.1 \$ g^{-1}	Adamas		
	MeCN	0.0087 mL^{-1}	Sigma-Aldrich		
	CH_3OH	0.0031 \$ mL^{-1}	Sigma-Aldrich		
spe-MOF	$ZrCl_4$	0.06	Greagent	98.7 \$ g^{-1}	[34]
	H_3TATAB	15.0 \$ g^{-1}	Adamas		
	DMF	0.018 \$ mL^{-1}	Sigma-Aldrich		
	Trifluoroacetic acid	0.11 \$ mL^{-1}	Sigma-Aldrich		
	Acetic acid	0.0083 \$ mL^{-1}	Sigma-Aldrich		
	n-pentanol	0.015	Sigma-Aldrich		
$[Zn_2(oba)_2(dmimpym)]$	$Zn(NO_3)_2·6H_2O$	0.055 \$ g^{-1}	Greagent	401.3 \$ g^{-1}	[27]
	Dmimpym	166.7 \$ g^{-1}	Adamas		
	Oba	0.14 \$ g^{-1}	Adamas		
	CH_3OH	0.0031 \$ mL^{-1}	Sigma-Aldrich		
	DMA	0.0058 \$ mL^{-1}	Sigma-Aldrich		
$[Cu_3(OH)_2(Me_2BPZ)_2]$	Cu_2O	0.051 \$ g^{-1}	Greagent	317.3 \$ g^{-1}	[30]
	H_2Me_2BPZ	141.6 \$ g^{-1}	Adamas		
	NH_4OH	0.0036 \$ mL^{-1}	Sigma-Aldrich		
	C_2H_5OH	0.0072 \$ mL^{-1}	Sigma-Aldrich		
Mn-dtzip	$MnCl_2·4H_2O$	0.0079 \$ g^{-1}	Greagent	319.8 \$ g^{-1}	[23]
	H_4dtzip	326.4 \$ g^{-1}	Adamas		
	DMF	0.018 \$ mL^{-1}	Sigma-Aldrich		
	HNO_3	0.025 \$ mL^{-1}	Sigma-Aldrich		

Note: The calculation of the MOFs synthesis price is based on existing research[21,24]. The synthesis cost of MOFs is mainly comprised of the subsequent components: the raw material costs and equipment costs and process costs as well as labor costs. Among the above components, organic ligands, metal salts, and solvents, which are basic raw materials toward MOF synthesis, account for a primary proportion of the total synthesis cost. Then, our calculations do not take into account the operating costs and utility costs of

hydrothermal reactions, filtration, and drying. The rough cost ($ g^{-1}) of MOFs is calculated as follows: (organic ligand price ×organic ligand dosage + metal salt price ×metal salt dosage + solvent price ×solvent dosage)/(theoretical quality of MOFs ×yield). The lowest prices of the main raw materials for synthesis that can be provided by commercial suppliers in China are quoted and calculated.

References

[1] C. Qu, Y. Jiao, B. Zhao, D. C. Chen, R. Q. Zou, K. S. Walton, M. L. Liu, Nickel-based pillared MOFs for high-performance supercapacitors: design, synthesis and stability study, Nano Energy. 26 (2016) 66-73.

[2] B. Arstad, H. Fjellvåg, K. O. Kongshaug, O Swang, R. Blom, Amine functionalised metal organic frameworks (MOFs) as adsorbents for carbon dioxide, Adsorption 14 (2008) 755-762.

[3] M. Guo, H. Wu, L. Lv, H. Meng, J. Yun, J. Jin, J. Mi, A highly efficient and stable composite of polyacrylate and metal-organic framework prepared by interface engineering for direct air capture, ACS Appl. Mater. Interfaces. 13 (2021) 21775-21785.

[4] J. Toth, Uniform interpretation of gas/solid adsorption. Adv. Colloid Interface Sci. 55 (1995) 1-239.

[5] D. D. Do, Adsorption analysis: equilibria and kinetics, Imperial College Press, London, 1998.

[6] A. L. Myers, J. M. Prausnitz, Thermodynamics of mixed-gas adsorption, AIChE J. 11 (1965) 121-127.

[7] K. S. Walton, D. S. Sholl, Predicting multicomponent adsorption: 50 years of the ideal adsorbed solution theory, AIChE J. 61 (2015) 2757-2762.

[8] L. Li, R.-B. Lin, R. Krishna, H. Li, S. Xiang, H. Wu, J. Li, W. Zhou, B. Chen, Ethane/ethylene separation in a metal-organic framework with iron-peroxo sites, *Science* 362 (2018) 443-446,

[9] Y.-L. Peng, T. Wang, C. Jin, C.-H. Deng, Y. Zhao, W. Liu, K. A. Forrest, R. Krishna, Y. Chen, T. Pham, B. Space, P. Cheng, M. J. Zaworotko, Z. Zhang*, Nat. Commun*. 12 (2021) 1-8.

[10] D. Dubbeldam, S. Calero, D. E. Ellis, R. Q. Snurr, RASPA: molecular simulation software for adsorption and diffusion in flexible nanoporousmaterials, Mol. Simul. 42 (2016) 81-101.

[11] A. K. Rappe, C. J. Casewit, K. S. Colwell, W. A. Goddard III, W. M. Skiff, UFF, a full periodic table force field for molecular mechanics and molecular dynamics simulations, J. Am. Chem. Soc. 114 (1992) 10024-10035.

[12] M. G. Martin, J. I. Siepmann, Transferable potentials for phase equilibria. 1. united-atom description of n-alkanes, J. Phys. Chem. B. 102 (1998) 2569-2577.

[13] J. VandeVondele, M. Krack, F. Mohamed, M. Parrinello, T. Chassaing, J. Hutter, Quickstep: Fast and accurate density functional calculations using a mixed Gaussian and plane waves approach, Comput. Phys. Commun. 167 (2005) 103-128.

[14] S. Goedecker, M. Teter, J. Hutter, Separable dual-space gaussian pseudopotentials, Phys. Rev. B. 54 (1996) 1703-1710.

[15] C. Hartwigsen, S. Goedecker, J. Hutter, Relativistic separable dual-space gaussian pseudopotentials from H to Rn, Phys. Rev. B. 58 (1998) 3641-3662.

[16] S. Grimme, J. Antony, S. Ehrlich, H. Krieg, A consistent and accurate ab initio parametrization of density functional dispersion correction (DFT-D) for the 94 elements H-Pu, J. Chem. Phys. 132 (2010) 154104.

[17] T. Lu, F. Chen, Multiwfn: A multifunctional wavefunction analyzer, J Comput Chem. 33 (2012) 580-592.

[18] C. Lefebvre, G. Rubez, H. Khartabil, J.-C. Boisson, J. Contreras-García, E. Hénon, Accurately extracting the signature of intermolecular interactions present in the NCI plot of the reduced density gradient versus electron density, Phys. Chem. Chem. Phys. 2017 (19) 17928.

[19] W. Humphrey, A. Dalke, K. Schulten, VMD: visual molecular dynamics, J. Mol. Graph. Model. 14 (1996) 33-38.

[20] Z. Di, Z. Ji, C. Chen, R. Krishna, D. Yuan, M. Hong, M. Wu, Efficient separation of methanol-to-olefins products using a metal-organic framework with supramolecular binding sites, Chem. Eng. J.493 (2024) 152442.

[21] G.-D. Wang, Y.-Z. Li, R. Krishna, W.-Y. Zhang, L. Hou, Y.-Y. Wang, Z. Zhu, Scalable synthesis of robust MOF for challenging ethylene purification and propylene recovery with record productivity, Angew. Chem. Int. Ed. 136 (2024) e202319978.

[22] G.-D. Wang, Y.-Z. Li, W.-J. Shi, L. Hou, Y.-Y. Wang, Z. Zhu, Active sites decorated nonpolar pore-based MOF for one-step acquisition of C_2H_4 and recovery of C_3H_6, Angew. Chem. Int. Ed. 62 (2023) e202311654.

[23] L. Zhang, L.-N. Ma, G.-D. Wang, L. Hou, Z. Zhu, Y.-Y. Wang, A new honeycomb MOF

for C_2H_4 purification and C_3H_6 enrichment by separating methanol to olefin products, J. Mater. Chem. A. 11 (2023) 2343-2348.

[24] G.-D. Wang, Y.-Z. Li, H. Zeng, L. Hou, W. Lu, D. Li, Leveraging surface polarity in a cost-effective metal-organic framework for olefin purification from methanol-to-olefin products, Adv. Funct. Mater. (2025), 2504916.

[25] H. Li, Y. Zhou, C. Chen, Y. Li, Z. Liu, M. Wu, M. Hong, A Stable layered microporous MOF assembled with Y-O chains for separation of MTO products, Inorg. Chem. 63 (2024) 21548-21554.

[26] S. Gao, C. G. Morris, Z. Lu, Y. Yan, H. G. W. Godfrey, C. Murray, C. C. Tang, K. M. Thomas, S. Yang, M. Schröder, Selective hysteretic sorption of light hydrocarbons in a flexible metal-organic framework material, Chem. Mater. 28 (2016) 2331-2340.

[27] Y.-Z. Li, G.-D. Wang, R. Krishna, Q. Yin, D. Zhao, J. Qi, Y. Sui, L. Hou, A separation MOF with O/N active sites in nonpolar pore for one-step C_2H_4 purification from C_2H_6 or C_3H_6 mixtures, Chem. Eng. J. 466 (2023) 143056.

[28] W. Fan, X. Wang, X. Zhang, X. Liu, Y. Wang, Z. Kang, F. Dai, B. Xu, R. Wang, D. Sun, Fine-tuning the pore environment of the microporous Cu-MOF for high propylene storage and efficient separation of light hydrocarbons, ACS Cent. Sci. 5 (2019) 1261-1268.

[29] G.-D. Wang, R. Krishna, Y.-Z. Li, Y.-Y. Ma, L. Hou, Y.-Y. Wang, Z. Zhu, Rational construction of ultrahigh thermal stable MOF for efficient separation of MTO products and natural gas, ACS Materials Lett. 5 (2023) 1091-1099.

[30] G. Zhen, Y. Liu, Y. Zhou, Z. Ji, H. Li, S. Zou, W. Zhang, Y. Li, Y. Liu, C. Chen, M. Wu, Water-stable microporous bipyrazole-based framework for efficient separation of MTO products, ACS Appl. Mater. Interfaces. 16 (2024) 1179-1186.

[31] W. Wei, X. Guo, Z. Zhang, Y. Zhang, D. Xue, Topology-guided synthesis and construction of amide-functionalized rare-earth metal-organic frameworks, Inorg. Chem. Commun. 133 (2021) 108896.

[32] D. Geng, M. Zhang, X. Hang, W. Xie, Y. Qin, Q. Li, Y. Bi, Z. Zheng, A 2D metal-thiacalix[4]arene porous coordination polymer with 1D channels: gas absorption/separation and frequency response, Dalton Trans. 47 (2018) 9008-9013.

[33] X.-H. Han, K. Gong, X. Huang, J.-W. Yang, X. Feng, J. Xie, B. Wang, Syntheses of covalent organic frameworks via a one-pot suzuki coupling and schiff's base reaction for C_2H_4/C_3H_6 separation, Angew. Chem. Int. Ed. 61 (2022) e202202912.

[34] H. Fang, B. Zheng, Z.-H. Zhang, H.-X. Li, D.-X. Xue, J. Bai, Ligand-conformer-induced formation of zirconium-organic framework for methane storage and MTO product separation, Angew. Chem. Int. Ed. 60 (2021) 16521-16528.

[35] Y. Zhang, X.-Q. Meng, H.-J. Ding, X. Wang, M.-H. Yu, S.-M. Zhang, Z. Chang, X.-H. Bu, Rational construction of breathing metal-organic frameworks through synergy of a stretchy ligand and highly variable π-π interaction, ACS Appl. Mater. Interfaces. 11 (2019) 20995-21003.

[36] X. Liu, C. Hao, J. Li, Y. Wang, Y. Hou, X. Li, L. Zhao, H. Zhu, W. Guo, An anionic metal-organic framework: metathesis of zinc(II) with copper(II) for efficient C_3/C_2 hydrocarbon and organic dye separation, Inorg. Chem. Front. 5 (2018) 2898-2905.

[37] W. Fan, Y. Wang, Q. Zhang, A. Kirchon, Z. Xiao, L. Zhang, F. Dai, R. Wang, D. Sun, An amino-functionalized metal-organic framework, based on a rare $Ba_{12}(COO)_{18}(NO_3)_2$ cluster, for efficient $C_3/C_2/C_1$ separation and preferential catalytic performance, Chem. Eur. J. 24 (2018) 2137-2143.

[38] C.-X. Chen, Z.-W. Wei, Q.-F. Qiu, Y.-Z. Fan, C.-C. Cao, H.-P. Wang, J.-J. Jiang, D. Fenske, C.-Y. Su, A porous Zn(II)-metal-organic framework constructed from fluorinated ligands for gas adsorption, Cryst. Growth Des. 17 (2017) 1476-1479.

[39] W. Su, A. Zhang, Y. Sun, M. Ran, X. Wang, Adsorption properties of C_2H_4 and C_3H_6 on 11 adsorbents, J. Chem. Eng. Data. 62 (2017) 417-421.

[40] J.-X. Wang, T.-F. Zhang, J. Pei, D. Liu, Y.-B. Wang, X.-W. Gu, G. Qian, B. Li, An MOF-based single-molecule propylene nanotrap for benchmark propylene capture from ethylene, Chem Bio Eng. 1 (2024) 952-959.

[1] C. Qu, Y. Jiao, B. Zhao, D. C. Chen, R. Q. Zou, K. S. Walton, M. L. Liu, Nickel-based pillared MOFs for high-performance supercapacitors: design, synthesis and stability study, Nano Energy. 26 (2016) 66-73.

[2] J. Toth, Uniform interpretation of gas/solid adsorption. Adv. Colloid Interface Sci. 55 (1995) 1-239.

[3] D. D. Do, Adsorption analysis: equilibria and kinetics, Imperial College Press, London, 1998.

[4] A. L. Myers, J. M. Prausnitz, Thermodynamics of mixed-gas adsorption, AIChE J. 11 (1965) 121-127.

[5] K. S. Walton, D. S. Sholl, Predicting multicomponent adsorption: 50 years of the ideal adsorbed solution theory, AIChE J. 61 (2015) 2757-2762.

[6] D. Dubbeldam, S. Calero, D. E. Ellis, R. Q. Snurr, RASPA: molecular simulation software for adsorption and diffusion in flexible nanoporousmaterials, Mol. Simul. 42 (2016) 81-101.

[7] A. K. Rappe, C. J. Casewit, K. S. Colwell, W. A. Goddard III, W. M. Skiff, UFF, a full periodic table force field for molecular mechanics and molecular dynamics simulations, J. Am. Chem. Soc. 114 (1992) 10024-10035.

[8] M. G. Martin, J. I. Siepmann, Transferable Potentials for Phase Equilibria. 1. United-Atom Description of n-Alkanes, J. Phys. Chem. B. 102 (1998) 2569-2577.

[9] J. VandeVondele, M. Krack, F. Mohamed, M. Parrinello, T. Chassaing, J. Hutter, Quickstep: Fast and accurate density functional calculations using a mixed Gaussian and plane waves approach, Comput. Phys. Commun. 167 (2005) 103-128.

[10] S. Goedecker, M. Teter, J. Hutter, Separable dual-space Gaussian pseudopotentials, Phys. Rev. B. 54 (1996) 1703-1710.

[11] C. Hartwigsen, S. Goedecker, J. Hutter, Relativistic separable dual-space Gaussian pseudopotentials from H to Rn, Phys. Rev. B. 58 (1998) 3641-3662.

[12] S. Grimme, J. Antony, S. Ehrlich, H. Krieg, A consistent and accurate ab initio parametrization of density functional dispersion correction (DFT-D) for the 94 elements H-Pu, J. Chem. Phys. 132 (2010) 154104.

[13] T. Lu, F. Chen, Multiwfn: A multifunctional wavefunction analyzer, J Comput Chem. 33 (2012) 580-592.

[14] C. Lefebvre, G. Rubez, H. Khartabil, J.-C. Boisson, J. Contreras-García, E. Hénon, Accurately extracting the signature of intermolecular interactions present in the NCI plot of the reduced density gradient versus electron density, Phys. Chem. Chem. Phys. 2017 (19) 17928.

[15] W. Humphrey, A. Dalke, K. Schulten, VMD: Visual molecular dynamics, J. Mol. Graph. Model. 14 (1996) 33-38.

[16] G.-D. Wang, Y.-Z. Li, R. Krishna, W.-Y. Zhang, L. Hou, Y.-Y. Wang, Z. Zhu, Scalable Synthesis of Robust MOF for Challenging Ethylene Purification and Propylene Recovery with Record Productivity, Angew. Chem. Int. Ed, 2024, 136, e20231997.

[17] L. Zhang, L.-N. Ma, G.-D. Wang, L. Hou, Z. Zhu, Y.Y. Wang, A new honeycomb MOF for C_2H_4 purification and C_3H_6 enrichment by separating methanol to olefin products, J. Mater. Chem. A 11 (2023) 2343-2348.

[18] H. Li, Y. Zhou, C. Chen, Y. Li, Z. Liu, M. Wu, M. Hong, A Stable Layered Microporous MOF Assembled with Y-O Chains for Separation of MTO Products, Inorg. Chem. 63 (2024) 21548-21554.

[19] S. Gao, C. G. Morris, Z. Lu, Y. Yan, H. G. W. Godfrey, C. Murray, C. C. Tang, K. M. Thomas, S. Yang, M. Schröder, Chem. Mater. 28 (2016) 2331-2340.

[20] Y.-Z. Li, G.-D. Wang, R. Krishna, Q. Yin, D. Zhao, J. Qi, Y. Sui, L. Hou, A separation MOF with O/N active sites in nonpolar pore for One-step C_2H_4 purification from C_2H_6 or C_3H_6 mixtures, Chem. Eng. J. 466 (2023) 143056.

[21] W. Fan, X. Wang, X. Zhang, X. Liu, Y. Wang, Z. Kang, F. Dai, B. Xu, R. Wang, D. Sun, Fine-tuning the pore environment of the microporous Cu-MOF for high propylene storage and efficient separation of light hydrocarbons, ACS Cent. Sci. 5 (2019) 1261-1268.

[22] G.-D. Wang, R. Krishna, Y.-Z. Li, Y.-Y. Ma, L. Hou, Y.-Y. Wang, Z. Zhu, Rational Construction of Ultrahigh Thermal Stable MOF for Efficient Separation of MTO Products and Natural Gas, ACS Materials Lett. 5 (2023) 1091-1099.

[23] W. Wei, X. Guo, Z. Zhang, Y. Zhang, D. Xue, Topology-guided synthesis and

construction of amide-functionalized rare-earth metal–organic frameworks, Inorg. Chem. Commun. 133 (2021) 108896.

[24] D. Geng, M. Zhang, X. Hang, W. Xie, Y. Qin, Q. Li, Y. Bi, Z. Zheng, A 2D metal-thiacalix[4]arene porous coordination polymer with 1D channels: gas absorption/separation and frequency response, Dalton Trans. 47 (2018) 9008-9013.

[25] X.-H. Han, K. Gong, X. Huang, J.-W. Yang, X. Feng, J. Xie, B. Wang, Syntheses of Covalent Organic Frameworks via a One-Pot Suzuki Coupling and Schiff's Base Reaction for C_2H_4/C_3H_6 Separation, Angew. Chem. Int. Ed. 61 (2022) e202202912.

[26] H. Fang, B. Zheng, Z.-H. Zhang, H.-X. Li, D.-X. Xue, J. Bai, Ligand-Conformer-Induced Formation of Zirconium-Organic Framework for Methane Storage and MTO Product Separation, Angew. Chem. Int. Ed. 60 (2021) 16521-16528.

[27] Y. Zhang, X.-Q. Meng, H.-J. Ding, X. Wang, M.-H. Yu, S.-M. Zhang, Z. Chang, X.-H. Bu, Rational Construction of Breathing Metal-Organic Frameworks through Synergy of a Stretchy Ligand and Highly Variable π-π Interaction, ACS Appl. Mater. Interfaces. 11 (2019) 20995-21003.

[28] X. Liu, C. Hao, J. Li, Y. Wang, Y. Hou, X. Li, L. Zhao, H. Zhu, W. Guo, An anionic metal-organic framework: metathesis of zinc(II) with copper(II) for efficient C_3/C_2 hydrocarbon and organic dye separation, Inorg. Chem. Front. 5 (2018) 2898-2905.

[29] W. Fan, Y. Wang, Q. Zhang, A. Kirchon, Z. Xiao, L. Zhang, F. Dai, R. Wang, D. Sun, An Amino-Functionalized Metal-Organic Framework, Based on a Rare $Ba_{12}(COO)_{18}(NO_3)_2$ Cluster, for Efficient $C_3/C_2/C_1$ Separation and Preferential Catalytic Performance, Chem. Eur. J. 24 (2018) 2137-2143.

[30] C.-X. Chen, Z.-W. Wei, Q.-F. Qiu, Y.-Z. Fan, C.-C. Cao, H.-P. Wang, J.-J. Jiang, D. Fenske, C.-Y. Su, A Porous Zn(II)-Metal-Organic Framework Constructed from Fluorinated Ligands for Gas Adsorption, Cryst. Growth Des. 17 (2017) 1476-1479.

[31] W. Su, A. Zhang, Y. Sun, M. Ran, X. Wang, Adsorption Properties of C_2H_4 and C_3H_6 on 11 Adsorbents, J. Chem. Eng. Data. 62 (2017) 417-421.

1

2

3